Chemistry Europe
European Chemical Societies Publishing
Batteries & Supercaps

RESEARCH ARTICLE OPEN ACCESS

# Scaling up Battery-Electrode Drying from Lab to Pilot Scale: Match the Drivers, Not the Set Points

Max-Wolfram von Horstig[1,2] | Julian Borho[3] | Jonas Mohacsi[3] | Philip Scharfer[3] | Peter Michalowski[1,2] | Wilhelm Schabel[3] | Arno Kwade[1,2]

[1]Institute for Particle Technology, Technische Universität Braunschweig, Braunschweig, Germany | [2]Battery LabFactory Braunschweig, Technische Universität Braunschweig, Braunschweig, Germany | [3]Institute of Thermal Process Engineering, Thin Film Technology, Karlsruhe Institute of Technology, Karlsruhe, Germany

**Correspondence:** Max-Wolfram von Horstig (m.von-horstig@tu-braunschweig.de)

**Received:** 30 October 2025 | **Revised:** 17 February 2026 | **Accepted:** 18 February 2026

**Keywords:** battery | drying | electrodes | modeling | scale-up

## ABSTRACT

Ramping up new products or equipment for the production of electrodes for lithium-ion batteries can be very challenging. Even when process parameters have been derived at the laboratory or pilot scale, transferring them to industrial-scale machines can present additional challenges that can be costly in terms of time and money. This paper presents a physics-based drying model developed to describe the drying behavior of anode coatings in convective roll-to-roll pilot plant dryers. To this end, a dryer air condition model and an electrode-drying model were coupled to accurately predict the entire process. Drying kinetics were measured and compared between two pilot plants and a laboratory dryer. The results demonstrate that the model can accurately describe the complete temperature profile of the wet film and predict the exhaust-air dew point with precision across both pilot plant machines. The mean heat-transfer coefficient was identified as a physical parameter with which to compare the ventilation settings of different dryers, allowing for the transfer of machine parameters between different roll-to-roll machines. This tool can be used to shorten ramp-up phases or to transfer complex drying profiles or new electrode recipes from the lab to the pilot or industrial scale.

## 1 | Introduction

Energy storage systems, particularly lithium-ion batteries, are central to the global transition toward electrified mobility and renewable energy integration. As battery production capacity scales rapidly, reducing manufacturing costs and energy demand while ensuring high product quality has become a major industrial and scientific challenge. In lithium-ion battery cell production, drying the electrodes accounts for 27–40% of the total energy required for battery production and requires large machines with important implications for the economics of the entire battery production process [1, 2]. Furthermore, the drying process is important for electrode quality, as high drying rates are associated with segregation effects that negatively impact the mechanical stability and electrochemical performance of the electrode coatings [3, 4]. Approaches to address this optimization tradeoff between throughput and product quality include multilayer coating [5, 6]; the use of carbon nanotubes [7, 8] or vapor-grown carbon fibers [9]; reducing the solvent content [10]; activation or precoating of metal foil substrates [11, 12]; innovative drying technologies such as infrared, laser, or induction heating [13–17]; and multistage drying profiles [18]. Although lab-scale studies reveal significant improvements in terms of process speed, specific energy demand, and electrode quality, it can be challenging to implement these results in industry. Lab-scale processes may differ from roll-to-roll machines in that they allow for more precise control of process conditions, which is not always possible in production. Pilot machines can be an effective means of improving transferability, as all of the main processes are similar to

those on an industrial scale [19]. However, challenges remain for a direct translation of the process parameters. The lack of understanding of the mechanistic impact of the machines' drying control parameters may lead to additional costly interruptions. This is particularly the case when a product change occurs, for example, when testing a new slurry chemistry or formulation.

Transferring an established electrode drying recipe from one coating line to another reveals a cascade of interdependent challenges that extends far beyond merely copying setpoints. The drying process is governed by two main metrics (film temperature and drying rate), which together influence binder migration, particle consolidation, and ultimately the electrodes' pore structure, mechanical integrity, and electrochemical performance [3, 4, 13, 20–23]. The drying rate, often expressed as a mass flux, needs to be set to balance evaporation and diffusion inside the electrode film and, in that regard, to prevent gradient formation of inactive components. The film temperature influences vapor pressure at the electrodes' surface and impacts diffusion, critically affecting the electrode quality [13, 24, 25]. These core metrics are controlled by a handful of physical levers, namely, the heat- and mass-transfer coefficients, the temperature of the dryer air, and its humidity. These factors are decisive for the vapor pressure gradient between the film and the dryer air and thereby govern the drying rate [21, 22].

At the machine level, the control of these factors is not directly possible. The most straightforward factor is the dryer air temperature. Most machines allow setting the temperatures directly at the control panel. While small deviations due to control variations may occur, this parameter can overall be controlled precisely. However, the air temperature at both ends of the drying chamber can be significantly lower than the set value. Dryers operate at a lower pressure to prevent solvents from leaking out of the machine. This leads to the suction of colder ambient air at the ends of the dryer, which reduces the air temperature in the first and last segments. While industrial-scale dryers, often up to 100 m long, are less affected, a significant fraction of the dryers can be affected in pilot plants. The moisture content of dryer air depends on several factors. In systems that use only fresh air, the moisture content of the dryer air is similar to that of the supply air. In laboratory dryer setups, this is often equal to the ambient moisture in the laboratory, which can vary depending on the time of day and local weather conditions. To save energy, larger roll-to-roll dryers typically use a circulating air stream that only partially exchanges with the supply air in order to prevent moisture saturation. However, the moisture content of the circulating dryer air in these machines is higher than that of the supply air, as evaporated solvent accumulates in the drying chamber. While some dryers allow for the preconditioning of supply air, which prevents seasonal differences, the moisture level in the dryer air still depends on the amount of fresh air and evaporation rate, making it hard to control directly. The heat- and mass-transfer coefficients combine the many influences of airflow distribution, turbulence intensity, and boundary-layer thickness. Local nuances of the dryer, such as nozzle count, nozzle orientation, nozzle geometry, and chamber aspect ratio, all contribute to the heat- and mass-transfer coefficients experienced by the coating. Therefore, nominal parameters such as fan speeds, fan power, or volumetric flow rate, which are common control parameters for the operator, cannot fully capture the thermodynamic kinetics applied to the web. A further challenge in the transferability of drying processes arises from the locally varying structural characteristics of the dryer, which lead to nonuniform drying conditions within the drying chambers. In particular, the heat and consequently the mass-transfer coefficients strongly depend on the position inside the dryer. Due to variations in nozzle spacing and number, a spatially changing heat-transfer coefficient profile is established, exhibiting pronounced minima and maxima with differences of several hundred W $m^{-2}$ $K^{-1}$ beneath and between the nozzles [26]. The impact of such heat-transfer coefficient profiles on the resulting electrode properties has not yet been investigated in the literature. Overcoming these challenges in scaling up and transferring drying processes requires a shift from "duplicating the set points" to "matching the driving forces."

Model-based approaches for accelerating electrode-drying process development by reducing experimental trial iterations have been proposed in several studies [21, 27, 28]. However, the predictive accuracy of these drying simulations strongly depends on precise knowledge of the equipment-specific heat-transfer coefficients. Obtaining these coefficients is particularly challenging, as they typically require detailed and computationally expensive computational fluid dynamics (CFD) simulations [26, 29]. Additionally, many of these models assume fixed values for environmental boundary conditions, such as supply air humidity, even though these parameters cannot be controlled with the same precision in pilot-scale equipment.

This work addresses this gap by directly comparing two industrially relevant pilot-scale dryers with a lab-scale drying setup under controlled conditions. Anode coatings are produced across the three drying setups with various parameter settings, and the drying kinetics are measured and compared. A combined model for the dryer air conditions and the electrode drying is proposed and parameterized with the experimental results. From the model, a correlation between the machines' air flow control parameters and a lumped mean convective heat-transfer coefficient is derived. This coefficient provides a physically grounded, machine-independent descriptor of drying intensity, enabling consistent adjustment of drying conditions across different equipment types. Such a unified parameter offers a practical route toward improving the robustness of process transfers, reducing commissioning time, and minimizing scrap during material development or product changes.

## 2 | Experimental Section

### 2.1 | Experimental

#### 2.1.1 | Slurry Preparation

For the experimental investigations, 5.5 L of anode suspension was produced for each trial in a planetary mixer (PMH10 by Netzsch). A setup of two tooth disks as a high-speed steerer (HSS), a cross-beam low-speed steerer (LSS), and a baffle, which rotates along the mixing vessel wall, was utilized. A dry mixture consisting of battery-grade natural graphite (d50 = 19 µm), conductive carbon black (C65, Imerys), and sodium carboxymethyl cellulose (CMC CRT 2000 PA, Texturecel, IFF) was produced in a tumble mixer and subsequently mixed with deionized water and kneaded for 1 h at an HSS speed of 2000 rpm and an LSS speed of 100 rpm. Finally, a 40 wt.% styrene-butadiene rubber (SBR BM-451B,

ZEON) solution was added, and the suspension was degassed under vacuum for half an hour at an HSS speed of 500 rpm and an LSS speed of 100 rpm. The final solids content was 50 wt.%. The compositions of the dry and wet mixtures are described in Table 1.

### 2.1.2 | Coating and Drying

The study utilized two convective roll-to-roll coating and drying machines at the pilot scale that differ slightly in dimensions, technology, and control parameters. The first machine, with a maximum web width of 350 mm, is the model KTF-S type 350 by Werner Mathis AG (referred to as Mathis machine). In Figure 1A, the Mathis machine is depicted as an example for a pilot-scale dryer, including the main control parameters for the drying process. The second pilot scale machine, with a maximum web width of 400 mm, is the model Kroenert Labco by Maschinenfabrik Max Kroenert GmbH & Co. KG (referred to as Kroenert machine). On a copper foil with a thickness of 10 µm and a width of 300 mm (Furukawa Electric), a wet film with a weight of 220 g $m^{-2}$ and a length of 10 m was applied at a web speed of 2 m $min^{-1}$. The Mathis machine applies the wet film with a doctor blade, while the Kroenert machine uses a comma-bar application system. Both machines have a total dryer section length of 6 m. However, the drying section of the Mathis machine is divided into six segments, each with a length of one meter and a volume of 0.45 $m^3$, while the drying section of the Kroenert machine is divided into three segments, each with a length of two meters and a volume of 1.4 $m^3$. The dryer air temperature of the ovens was set to 40 °C or 60 °C in all segments, and the fan speed was uniformly varied across all drying segments. For the Mathis machine, the circulating fan speed, $n_{fan}$, was set to a low setting of 1500 rpm and a high setting of 2500 rpm. For the Kroenert machine, three set points for the fan power, $P_{fan}$, were analyzed per temperature (with 60%, 80%, and 100% of the total fan power). The exhaust air flux of the dryers differs, with the Mathis machine exhausting 200 $m^3$ $h^{-1}$ of the circulating air from each segment, totaling 1320 $m^3$ $h^{-1}$, while the Kroenert machine exhausts 210 $m^3$ $h^{-1}$ per segment, totaling 630 $m^3$ $h^{-1}$. The fresh air supply of the Mathis machine was set to 200 $m^3$ $h^{-1}$ per segment, and the difference between the supply and the exhaust air is drawn in at the ends of the dryer. For the Kroenert machine, while not measured quantitatively, the supply air flux is also lower than the exhaust air flux. This is a common approach in electrode drying to prevent solvents from leaking out of the dryer into the ambient laboratory or factory atmosphere. The machine and process parameters of the two pilot dryers are compared in Table 2.

The Mathis machine is equipped with three infrared pyrometers (Optris CTex LT by Optris GmbH & Co. KG) in each drying segment to measure the film temperature and monitor the drying progress nondestructively inline. However, with only 18 measurement points distributed nonequidistantly along the dryer over a total drying time of 180 s, the mean measurement frequency during the drying process is equivalent to 0.1 Hz, which leads to some ambiguity in the evaluation. In addition, a type-K thermocouple (tolerance class 1) with a diameter of 2 x 0.08 mm (Therma

**TABLE 1** | Composition of the anode slurry's dry and wet mass.

| Anode | Dry mass content | Wet mass content |
|---|---|---|
| Graphite | 93.50 wt.% | 46.75 wt.% |
| Conductive carbon | 1.50 wt.% | 0.75 wt.% |
| Carboxymethyl cellulose | 1.66 wt.% | 0.83 wt.% |
| Styrene-butadiene rubber | 3.34 wt.% | 1.67 wt.% |
| Deionized water | 0.00 wt.% | 50.00 wt.% |

**TABLE 2** | Process parameters of the coating machines.

| parameter | Mathis | Kroenert |
|---|---|---|
| ambient dew point | 7.7°C | 3.2°C |
| coating device | doctor blade | comma bar |
| web speed | 2 m $min^{-1}$ | 2 m $min^{-1}$ |
| dry film weight | 105 g $m^{-2}$ | 115 g $m^{-2}$ |
| dry film coating thickness | 110 µm | 120 µm |
| coating width | 120 mm | 150 mm |
| no. segments | 6 | 3 |
| length of segments | 1 m | 2 m |
| volume of segment | 0.45 $m^3$ | 1.4 $m^3$ |
| exhaust air per segment | 220 $m^3$ $h^{-1}$ | 210 $m^3$ $h^{-1}$ |
| dryer air temperature | 40°C or 60°C | 40°C or 60°C |
| convection control | 1500 rpm or 2500 rpm | 60%, 80% or 100% |
| nozzle distance | 12 mm | 15 mm |

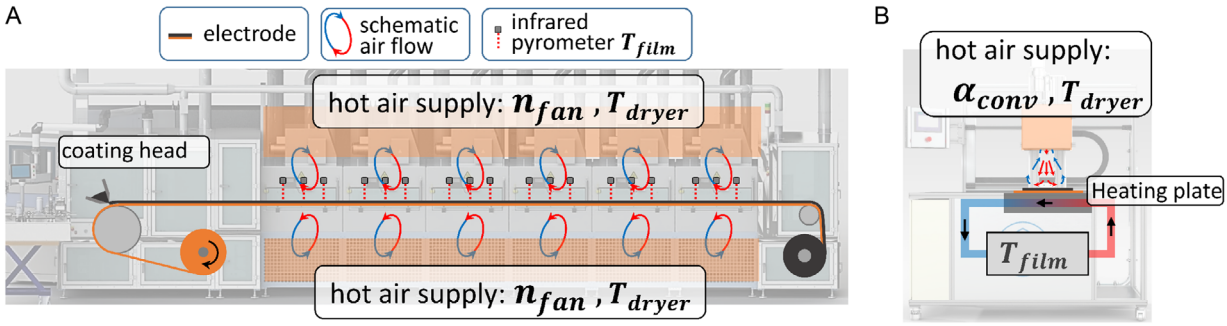


**FIGURE 1** | Three-dimensional renderings of the drying setups overlaid with schematic depictions of their main components and process parameters: (A) Mathis dryer at pilot scale (adapted under CC BY-NC 4.0 license [23]) and (B) Comb-Nozzle Dryer at laboratory scale.

Thermofühler GmbH) was placed into the wet coating from the top, fixed to the web with tape, and fed with the web through the dryer to obtain film temperature information with 1 Hz resolution. This approach was applied to the trials on both machines. The drying time was derived from the film temperature data by fitting a logistic growth model in a nonlinear regression and locating its inflection point to mark the end of drying, following the methodology described by von Horstig et al. [30] From solvent mass, $m_{A,s}$, and drying time, $t_{dry}$, the average drying rate, $\dot{m}_{A,dry}$, can be calculated. Solvent mass is estimated from dry electrode mass, $m_{A,el}$, and solids content, $x_{sc}$, leading to Equation (1).

$$\dot{m}_{A,dry} = \frac{m_{A,s}}{t_{dry}} = \frac{m_{A,el} \times \frac{1-x_{sc}}{x_{sc}}}{t_{dry}} \quad (1)$$

For the laboratory-scale drying experiments, a stationary dryer hood (Comb Nozzle Dryer, CN Drying Technology GmbH) and a temperature-controlled plate were used (Figure 1B). The drying experiments in this study were carried out under isothermal conditions. The laboratory dryer operates in batch mode and is based on the principle of convective drying. The drying conditions, and consequently the drying rate, can be precisely defined and reproduced by controlling the inlet air temperature and the heat-transfer coefficient. The heat-transfer coefficient, which is uniform across the entire nozzle field, can be adjusted by varying the airflow rate or the distance between the nozzle field and the substrate. The adjustable range of the heat-transfer coefficient is about 20–120 W $m^{-2}$ $K^{-1}$, while the air temperature can be varied between 20 °C and 150 °C. The substrate coating was performed using a doctor blade. Several publications by Kumberg et al. provide a comprehensive description of the Comb Nozzle Dryer and the coating procedure [21, 22]. Readers interested in further details regarding the setup and operation of the dryer are referred to these works. The applied heat-transfer coefficients and the inlet air and plate temperatures are provided in the supporting information (Chapter S1). The drying parameters applied in laboratory-scale experiments were chosen on the basis of the values predicted by the drying model for the investigated operating conditions of the Mathis dryer.

#### 2.1.3 | Dew Point

In addition, a dew point mirror (MBW Calibration 973 by Process Insights Inc.) was attached to the exhaust pipe of the second drying segment of the Mathis machine or the first segment of the Kroenert machine to measure the dew point of the exhaust air. At the beginning of the experiment, the moisture content of the exhaust air is equal to the moisture content of the supply air because there is not yet any wet film in the drying section that could lead to additional water vapor due to evaporation. The supply air is taken directly from the production hall so that the moisture content of the supply air is equal to the ambient moisture content, which was additionally compared to weather reports sourced from METAR EDVE/BWE (Braunschweig-Wolfsburg Airport; Deutscher Wetterdienst).

#### 2.1.4 | Adhesion Strength

As a quality control measure for the dry electrode, the adhesion strength was tested using a z-direction pull-off test (Z020 uniaxial tester by Zwick GmbH & Co. KG). Circular samples (12 mm diameter) were fixed between two stamps using double-sided tape. The test protocol applied a 68 N compressive preload for 30 s, immediately followed by a pull-off at 100 mm $s^{-1}$. The machine continuously records the force with a frequency of 100 Hz, and the highest pull-off load is taken as the adhesion force. Dividing this peak force by the cross-sectional area of the sample yields the adhesion strength. Each measurement was repeated with ten samples. Further procedural details are given in Haselrieder et al. [31].

#### 2.1.5 | Color Value

As a second measurement of electrode quality, the surface color was characterized using a handheld spectrophotometer (sPh900 by ColorLite GmbH). The device illuminates the sample and reports color values in the Commission Internationale de l'Éclairage (CIE) L*a*b* color space (CIE-Lab*). The results were analyzed with particular attention paid to the L* coordinate (lightness), which spans from 0 (black) to 100 (white). To ensure reproducibility, ten independent measurements were taken on each electrode. For a detailed procedural and principal description, see Weber & Schoo et al. [32].

### 2.2 | Drying Model

A sophisticated way to transfer drying parameters from one machine to another would be to set up a drying model, conduct several experiments to parameterize the model for both machines, and use the model to predict the parameters for the transfer. This helps to bridge the gap between machines with different control parameters, for example, when the circulating air flux is controlled by fan speed, fan power, or air volume flux. The model used in this paper is based on the approach by Kumberg et al., who proposed a model for a lab-scale drying setup for anodes [21, 22]. Some adaptations have been made to better describe the drying process in the pilot plant machines. The basic equations of the model will be explained in the following paragraphs. However, more details can be found in the Supporting Information and in the work by Kumberg et al. [21, 22] The variables used are depicted in Figure 2. The electrode-drying model, based on energy and mass balances, is numerically solved in time steps of 0.1 s. Under the assumption that the heat conduction within the electrode is much greater than the convective heat transfer into the electrode [21], the electrode film is represented as a homogeneous body with a film temperature, $T_{film}(t)$, a solvent mass loading, $m_{A,s}$, a metal substrate mass, $m_{A,sub}$, and a dry electrode mass, $m_{A,el}$. The model is set up and solved for a single coating on one side of the metal foil. In industry, the back of the foil is usually coated in a subsequent step involving a tandem coating setup or coated simultaneously with both coatings being dried in a dryer chamber with a floating web [33]. However, this does not change the principles applied, and the model can easily be adapted to account for different coating setups.

The energy balance describes the change in the film temperature with respect to the convective and radiative heat introduced from the top, $\dot{q}_{A,top}$, and the bottom, $\dot{q}_{A,bot}$, and with respect to the solvent evaporation rate, $\dot{m}_{A,s}$, multiplied by the heat of evaporation, $\Delta h_{v,s}$ (Equation (2)).

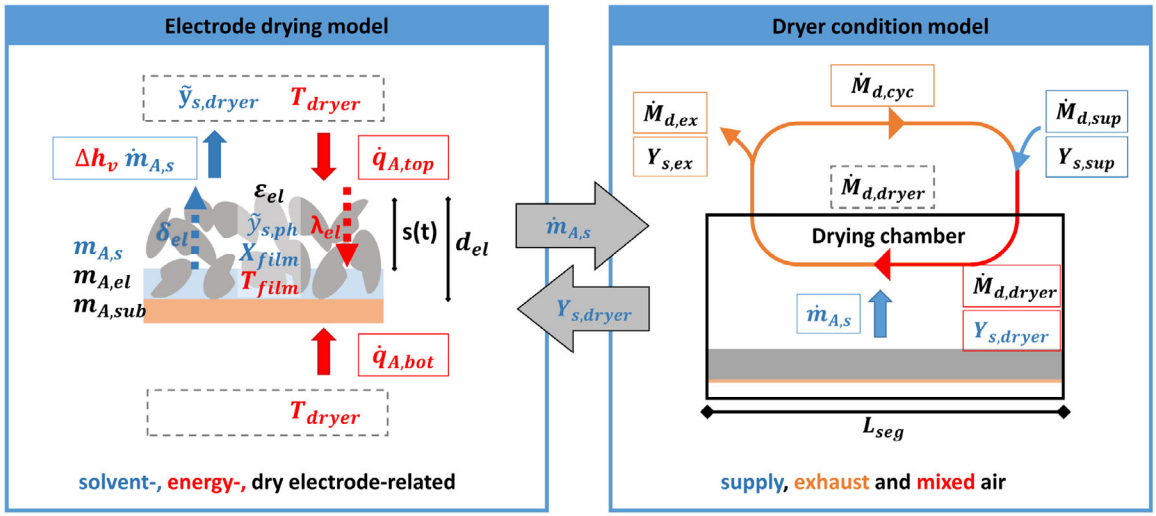


**FIGURE 2** | Schematic depiction of the two coupled models and the relevant parameters; the symbols are explained in the text upon occurrence and are denoted in the symbol list Table S5.

$$\frac{dT_{film}}{dt} = \frac{\dot{q}_{A,top} + \dot{q}_{A,bot} - \dot{m}_{A,s}\,\Delta h_{v,s}}{m_{A,el}\,c_{p,el} + m_{A,sub}\,c_{p,sub} + m_{A,s}\,c_{p,s}} \tag{2}$$

The area-specific heat flux from the top, $\dot{q}_{A,top}$, is calculated using Equation (3) by multiplying the top-side heat-transfer coefficient, $\alpha_{top,tot}$, and the difference in dryer air temperature, $T_{dryer}$, and film temperature, $T_{film}$ [21]. Further details on the heat-transfer coefficient and the correction factor can be found in the supporting information.

$$\dot{q}_{A,top} = \alpha_{top,tot}\,(T_{dryer} - T_{film}) \tag{3}$$

The heat-transfer coefficient consists of the radiative heat-transfer coefficient, $\alpha_{top,rad}$ and the convective heat-transfer coefficient, $\alpha_{top,conv}$, multiplied by the Ackermann correction factor, $K_A$, which takes into account the influence of the mass flux of the evaporating solvent on the heat flux (Equation (4)).

$$\alpha_{top,tot} = \alpha_{top,rad} + K_A\,\alpha_{top,conv} \tag{4}$$

While the radiative heat-transfer coefficient can be described by applying the Stefan-Boltzmann law to two parallel, plate-shaped gray bodies, predicting the convective heat-transfer coefficient is more difficult [21]. In a complex dryer geometry, detailed CFD simulations [34] or highly specific empirical correlations [29] are required to accurately depict the complex airflow and yield the corresponding field of heat-transfer coefficients. Both methods are time-consuming and prone to inaccurate assumptions. In addition, they require detailed knowledge of all the relevant geometries within the dryer to accurately model airflow. However, intellectual property protection and time-consuming measurements may hinder this approach.

In this study, therefore, a more practical simplification is proposed. A single mean convective heat-transfer coefficient, $\alpha_{conv,m}$ is identified iteratively for the entire dryer at homogeneous control-parameter settings by fitting the dryer model to experimental drying data. This "pseudo-physical" approach does not aim to reproduce the full spatial flow field as a CFD model would, but provides a fast and robust estimate of the effective heat transfer under the chosen operating conditions. While it sacrifices spatial resolution, it significantly reduces the modeling effort and still yields sufficient accuracy for averaged predictions. Furthermore, $\alpha_{conv,m}$ can absorb effects that are not fully resolved in the model, such as local flow nonuniformities or moisture gradients [26], which make it a practical lumped parameter.

To ensure that the model remains grounded in real convection physics, the quality of $\alpha_{conv,m}$ can be evaluated by checking how it changes when only the inlet air temperature or humidity is varied. In a well-posed model, $\alpha_{conv,m}$ should depend primarily on airflow conditions. Because dryer air temperature and moisture vary only within a narrow range, their influence on $\alpha_{conv,m}$ is expected to be small. Any significant systematic drift of $\alpha_{conv,m}$ within this restricted temperature-humidity space would indicate insufficient boundary conditions and thus define the limits of applicability. This criterion also provides guidance on the limitations and robustness of the lumped-parameter approach when applied to other dryer designs or operating scenarios.

The mass balance describes the area-specific mass of the evaporating solvent as a function of the mass-transfer coefficient $\beta_{s,air}$, the molar mass of the solvent $\tilde{M}_s$, the molar density of the air $\tilde{\rho}_{air}$, the functions for the molar fractions of the solvent in the gas phase of the dryer $\tilde{y}_{s,dryer}$, and at the interface $\tilde{y}_{s,ph}$, and the Stefan correction factor $K_{St}$, which takes into account the resulting drag flows [21].

$$\dot{m}_{A,s} = K_{St}\,\tilde{M}_s\,\beta_{s,air}\,\tilde{\rho}_{air}\,(\tilde{y}_{s,ph} - \tilde{y}_{s,dryer}) \tag{5}$$

The mass-transfer coefficient is proportional to the convective heat-transfer coefficient at the top via the Lewis analogy, with n equal to 0.42 for turbulent flow, considering the molar density of air, $\tilde{\rho}_{air}$, the molar heat capacity of air, $\tilde{c}_{p,air}$, and the molar heat capacity of the gaseous solvent $\tilde{c}_{p,s,g}$ [21].

$$\beta_{s,air} = \frac{\alpha_{top,conv}}{Le^{1-n}\,\tilde{\rho}_{air}\left[\tilde{c}_{p,air}\,(1-\tilde{y}_{s,dryer}) + \tilde{c}_{p,s,g}\,\tilde{y}_{s,dryer}\right]} \tag{6}$$

The model describes the drying process with regard to the vapor pressure gradient as the main driver and quantifies its effect on

the film temperature and film solvent content of the electrode. Eventually, once enough solvent has evaporated, the particles in the slurry come into contact and form a solvent-filled pore structure. Solvent evaporation continues after this characteristic time point, known as the "end of film shrinkage" (EOF). However, after EOF, the drying process enters a regime in which diffusion-related resistances take effect since heat and mass transfer must now proceed through the partially depleted pore structure. Kumberg et al. argue that this effect becomes significant with thick electrodes or at high drying rates when capillary-driven mass transport within the electrode film cannot maintain sufficient liquid coverage of the surface [22]. Kumberg et al. observed a significant impact in coatings with a dry electrode mass greater than 160 g $m^{-2}$ [22]. Although the coatings in this study are significantly lighter than those investigated by Kumberg et al., the drying rates are higher, which may lead to the observation of this effect, especially with more aggressive drying profiles. To represent the observed behavior, the equations for $\dot{m}_s$ and $\dot{q}_{A,top}$ have to be adapted. Under the assumption that a drying front moves simultaneously along the entire electrode from top to bottom, a series connection of heat and mass transport resistances is used to account for the additional heat and mass transport resistances in the partially dried electrode. The thickness of the dried section of the electrode is denoted by $s(t)$, and the additional heat and mass transport resistances are calculated by dividing this thickness by the thermal conductivity of the dry electrode $\lambda_{el}$ or the diffusion coefficient of the solvent in the dry electrode $\delta_{s,el}$, respectively. These adaptations lead to Equations (7) and (8) [22]. Further details on the calculation of these parameters can be found in the Supplementary Information. Notably, this assumption can be refuted based on the existing literature [21, 35]. However, this is a straightforward approach to the phenomenon of reduced drying rates in this phase of the process, which is why it was chosen.

$$\dot{q}_{A,top} = \frac{1}{\frac{1}{\alpha_{top,tot}} + \frac{s(t)}{\lambda_{el}}} \left(T_{dryer} - T_{film}\right) \tag{7}$$

$$\dot{m}_{A,s} = K_{St}\, \tilde{M}_s\, \frac{1}{\frac{1}{\beta_{s,air}} + \frac{s(t)}{\delta_{el}}}\, \tilde{\rho}_{air} \left(\tilde{y}_{s,ph} - \tilde{y}_{s,dryer}\right) \tag{8}$$

The first modification of the model concerns the mode of heat flux. Convective ($\dot{q}_{A,conv}$) and radiative ($\dot{q}_{A,rad}$) heat transfer at the top and bottom of the electrode are now included, representing the hot-air nozzles positioned above and below the moving web. Additionally, a dryer condition model has been introduced to capture changes in the circulating air's dew point caused by supply air humidity and solvent evaporation (Figure 2). The differences in ratio between the volume of a segment and the exhaust air volume flux per segment between the two compared dryers lead to different time constants for exchange of the dryer air. For the Mathis machine the air is exchanged on average every 7 s, while for the Kroenert machine it takes about 24 s to exchange the whole volume in the dryer segment at given machine parameters. At the same time, twice the amount of solvent evaporates per segment in the Kroenert machine due to its double length when the same drying rate is achieved. This affects the time needed for the dryer conditions to stabilize after the coating process begins. This is less important for industry-scale production that runs for several hours up to a whole week without interruption, but can affect the drying results in pilot machines, where often only a few meters of coating are produced per experiment. The time until equilibrium was reached is approximated to be 40 s for the Mathis machine and 120 s for the Kroenert machine for the selected parameters, which is well below the coating time (300 s) in our experiments. Details on the calculation can be found in the Supporting Information (Chapter S2).

To calculate the solvent content in the dryer air in the equilibrium state of the drying process, mass balances were set up. The solvent mass-mixing ratio of the exhaust $Y_{s,ex}$, and the supply air $Y_{s,sup}$, as well as their volume flux, can be measured directly in the piping of the dryer. The dryer air volume flux $\dot{V}_{dryer}$ depends on the fan speed and is calculated from the measured air velocities in the nozzles and their respective cross-sectional areas. This approach is an approximation, as the pilot plant dryers were not equipped with sensors to directly measure the dryer air volume flux during the drying process. The resulting correlations are given in Table 3. At a constant fan speed, the volumetric flow rate remains almost constant despite minor variations in temperature, humidity, or pressure because both the fan's pressure–flow curve and the pipe's friction–loss curve are proportional to air density [36]. Therefore, only one reference measurement is needed to describe the process. In order to calculate meaningful mass balances, the volume flux needs to be converted into a dry air mass flux. Following Equation (9), the volume flux $\dot{V}$ can be transferred into a dry air mass flux $\dot{M}_d$ by multiplying the dry air density $\rho_d$, where the dry air density is given by the ideal-gas law, subtracting the partial pressure of the solvent $p_s$ from the total pressure $p$ and dividing it by the dry air gas constant, $R_d$ (287.05 J $kg^{-1}$ $K^{-1}$) and the temperature T.

$$\dot{M}_d = \rho_d\, \dot{V} = \frac{p - p_s}{R_d\, T}\, \dot{V} \tag{9}$$

First, the steady-state dry-air mass balance equates the supplied dry-air mass flux, $\dot{M}_{d,sup}$, with the exhausted dry-air mass flux, $\dot{M}_{d,ex}$ (Equation (10)). Although the exhaust volumetric flux is slightly higher than the supply flux in order to maintain a slight underpressure in the drying chamber, any excess volume is drawn in as ambient air at the ends of the chamber. As the supply air and ambient air both originate from the ambient air in the research facility, their absolute moisture content is identical, and the total dry air mass flux remains unchanged. Consequently, the small ambient air term is ignored in all subsequent mass and energy balances.

**TABLE 3** | Empirical equations for the circulating air volume flux and the mean heat-transfer coefficient.

| Dryer | $\dot{V}_{dryer}$/m³ h⁻¹ | $\alpha_{conv,m}$/W m⁻² K⁻¹ | Parametrized for: |
|---|---|---|---|
| Mathis | $0.33\, n_{fan} - 96.92$ | $0.03\, n_{fan} + 30$ | 38 –51°C and 1500–2500 rpm |
| Kroenert | $8.47\, P_{fan} - 258.34$ | $0.55\, P_{fan} + 17.2$ | 40 –58°C and 60–100% |

$$\dot{M}_{\mathrm{d,\,sup}} = \dot{M}_{\mathrm{d,ex}} \tag{10}$$

Furthermore, two mass balances for the solvent are set up. The first solvent mass balance is given in Equation (11) and equates the solvent mass flux in the dryer air stream, $\dot{M}_{\mathrm{s,dryer}}$, with the sum of the solvent mass flux of the supplied air, $\dot{M}_{\mathrm{s,\,sup}}$, and the recycled air, $\dot{M}_{\mathrm{s,cyc}}$ (Figure 2). The three can be described by their dry-air mass flux and their solvent mass-mixing ratios, $Y_{\mathrm{s,\,sup}}$, $Y_{\mathrm{s,cyc}}$ and $Y_{\mathrm{s,dryer}}$, respectively. The dry-air mass flux of recycled air, $\dot{M}_{\mathrm{d,cyc}}$, is calculated as the difference of the dry-air mass flux of the dryer and the exhaust air stream. The solvent mass-mixing ratio of the recycled air is equal to that of the exhaust air.

$$\begin{gathered}\dot{M}_{\mathrm{s,\,sup}} + \dot{M}_{\mathrm{s,cyc}} = \dot{M}_{\mathrm{s,dryer}} \\ \dot{M}_{\mathrm{d,\,sup}}\ Y_{\mathrm{s,\,sup}} + \dot{M}_{\mathrm{d,cyc}}\ Y_{\mathrm{s,cyc}} = \dot{M}_{\mathrm{d,dryer}}\ Y_{\mathrm{s,dryer}} \\ \dot{M}_{\mathrm{d,\,sup}}\ Y_{\mathrm{s,\,sup}} + (\dot{M}_{\mathrm{d,dryer}} - \dot{M}_{\mathrm{d,ex}})\ Y_{\mathrm{s,ex}} = \dot{M}_{\mathrm{d,dryer}}\ Y_{\mathrm{s,dryer}}\end{gathered} \tag{11}$$

The second solvent mass balance is given in Equation (12) and equates the solvent mass flux exiting the drying chamber with the solvent mass flux entering the chamber via the dryer air stream and the evaporation mass flow, $\dot{M}_{\mathrm{s,evap}}$.

$$\dot{M}_{\mathrm{d,dryer}}\ Y_{\mathrm{s,dryer}} + \dot{M}_{\mathrm{s,evap}} = \dot{M}_{\mathrm{d,dryer}}\ Y_{\mathrm{s,ex}} \tag{12}$$

By solving the aforementioned mass balances, equations for the solvent mass-mixing ratios can be derived. The solvent mass-mixing ratio of the exhaust air stream can be described by Equation (13).

$$Y_{\mathrm{s,ex}} = Y_{\mathrm{s,\,sup}} + \frac{\dot{M}_{\mathrm{s,evap}}}{\dot{M}_{\mathrm{d,ex}}} \tag{13}$$

The solvent mass-mixing ratio of the dryer air stream can be derived from Equation (14).

$$Y_{\mathrm{s,dryer}} = Y_{\mathrm{s,\,sup}} + \frac{(\dot{M}_{\mathrm{d,dryer}} - \dot{M}_{\mathrm{d,ex}})\ \dot{M}_{\mathrm{s,evap}}}{\dot{M}_{\mathrm{d,ex}}\ \dot{M}_{\mathrm{d,dryer}}} \tag{14}$$

The evaporation mass flow in each dryer segment is calculated by iterating through the whole model five times. During the initial run, since the actual drying rates are not yet known, an approximate constant drying rate is used across the entire length of the dryer. Accordingly, the solvent mass flow can be approximated as the areal solvent loading, $m_{\mathrm{A,s}}$, multiplied by the width, $W_{\mathrm{el}}$, of the coating and the web speed, $v_{\mathrm{web}}$, and divided by the number of segments of the drying chamber,$n_{\mathrm{seg}}$ (Equation (15)).

$$\dot{M}_{\mathrm{s,evap}} = \frac{m_{\mathrm{A,s}}\ W_{\mathrm{el}}\ v_{\mathrm{web}}}{n_{\mathrm{seg}}} \tag{15}$$

For the subsequent runs, the solvent mass flow is calculated for each segment independently, based on the difference in the solvent content of the wet film at the start and end of each segment $\Delta m_{\mathrm{A,s,seg}}$ of the previous run, following Equation (16).

$$\dot{M}_{\mathrm{s,evap}} = \Delta m_{\mathrm{A,s,seg}}\ W_{\mathrm{el}}\ v_{\mathrm{web}} \tag{16}$$

Finally, the solvent mass-mixing ratio of the dryer air, $Y_{\mathrm{s,dryer}}$, can be translated into the molar fraction of moisture in the air, $\tilde{y}_{\mathrm{s,dryer}}$, using the molar masses of the air, $\tilde{M}_{\mathrm{air}}$, and the solvent, $\tilde{M}_{\mathrm{s}}$, leading to Equation (17) . The molar fraction is then passed to the electrode-drying model.

$$\tilde{y}_{\mathrm{s,dryer}} = \frac{Y_{\mathrm{s,dryer}}\ \tilde{M}_{\mathrm{air}}}{Y_{\mathrm{s,dryer}}\ \tilde{M}_{\mathrm{air}} + \tilde{M}_{\mathrm{s}}} \tag{17}$$

## 3 | Results and Discussion

### 3.1 | Modeling of Drying on a Pilot Plant Dryer

Figure 3 shows the film temperature measurements and modeling results overlaid. Although the film temperature measurements from the thermocouple and the pyrometers differ, especially for the dry electrode film, the overall shape and timing of the drying temperature curves are comparable. The differences in measured dry film temperatures cannot be fully explained. The emission coefficient of the electrode film changes during drying, making it challenging to achieve an accurate film temperature throughout the process. It is likely that incorrect settings with respect to the emission coefficient have caused the deviation in the measurements. For further investigation, the thermocouple data will be used as it has better resolution than the pyrometer measurements. Furthermore, the final film temperature measured by the thermocouple aligns more accurately with the actual measured dryer air temperature, $T_{\mathrm{act}}$. A thermocouple mounted in the dryer measured the actual dryer air temperature to be 38 °C and 51 °C, respectively, which was below the target. For the model, these lower dryer air temperatures were used to accurately describe the temperature curves of the experiments. A possible reason is faulty temperature control by the machine or leaky seals that let cold ambient air into the dryer from between the segments. After a heat-up phase, a period of constant temperature can be observed, during which the temperatures remain relatively steady at about 25 °C and 35 °C, depending on the set dryer air temperature. Finally, the temperature rises quickly until it reaches a plateau again. This rise indicates the end of the electrode drying, as discussed in previous publications [21, 23, 30]. The final electrode temperature is well below the 40 °C and 60 °C that were set for these experiments, but it matches well with the actual measured air temperature. A periodic drop in film temperature of up to 5 °C was detected every meter, corresponding to the point in time when the electrode web moves from one dryer segment to the next. Cold ambient air was drawn between the segments due to faulty sealing, which explains both the overall lower air temperature in the chamber and the periodic fluctuations in film temperature (Chapter S5).

To parameterize the model, the circulating air volume flux was measured at different fan speeds, and a linear regression of the flux versus the fan speed was carried out. The resulting correlation is presented in Table 3. This proportional relationship is expected since ventilation fans typically exhibit an approximately linear airflow-speed characteristic over their normal operating range [36]. The mean heat-transfer coefficient in the model was iteratively fitted to match the temperature profiles generated by the model to the experimentally determined temperature profiles of each trial. The aforementioned temperature fluctuations mainly introduce noise into the air temperature profile and can make the parameter fitting less stable. Between the segments, the

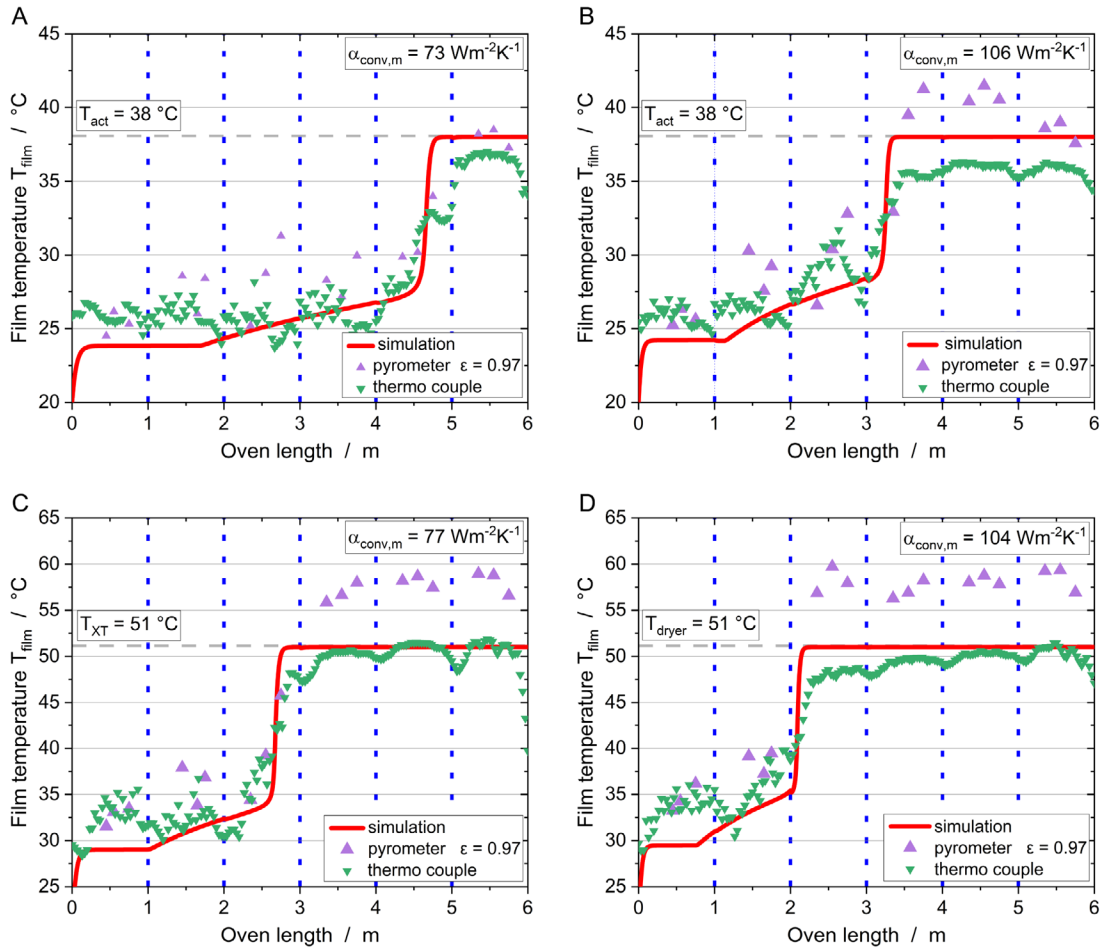


**FIGURE 3** | Film temperature for anode drying on the Mathis machine measured with infrared pyrometer and thermocouple and simulated with coupled drying model at iteratively selected $\alpha_{conv,m}$; variations of set points for $T_{dryer}$ and $n_{fan}$; (A,B) at 40°C and (C,D) 60°C (actual dryer air temperature was measured to be lower); (A,C) at 1500 rpm and (B,D) at 2500 rpm, indications of segments (blue).

distance between the drying nozzles is particularly wide at 40 cm, so the local heat-transfer coefficient in this region is relatively low. Since the temperature drop occurs in a region with inherently low convective heat- and mass-transfer, the influence on the mean convective heat-transfer coefficient is expected to be small. Therefore, the model remains reliable on an averaged level, as these fluctuations are effectively lumped into the fitted mean heat-transfer coefficient. If the overall lower air temperature caused by the leakage is taken into account, the model remains valid. However, after fixing the faulty sealing, a renewed parameterization may be necessary. This issue is not expected to limit its applicability to industrial dryers, where segment sealing is generally better.

Using these values for the mean heat-transfer coefficient reproduces the temperature profiles satisfactorily. After reaching the end of film shrinkage and entering a regime of pore emptying, a steady increase in film temperature can be observed in the model. Although less pronounced, this increase in film temperature can also be seen in some of the thermocouple measurements, especially at higher drying rates. However, the increase in film temperature near the end of film drying is much steeper in the model than in the experiments. This effect was also described in studies by Kumberg et al., on which the model is based [21, 22]. As possible explanations, they suggest uncertainties in the calculation of the heat conductivity of the partially filled pore network and the exclusion of lateral solvent transport [21, 22].

A functional relationship between the fan speed and the mean heat-transfer coefficient can be derived using linear regression. However, this linear fit of four data points only provides an approximation and does not accurately depict the more complex correlation between the two variables. Since the Reynolds number scales linearly with air velocity (and therefore with the fan speed in its normal operating range) and the Nusselt number (which is proportional to the convective heat-transfer coefficient) follows $Nu \propto Re^m$, it follows that the convective heat-transfer coefficient is expected to vary sub-linearly with the fan speed, specifically $\alpha_{conv} \propto n_{fan}^m$ (with $m < 1$) [36]. The presence of a nozzle field and the impingement of the nozzles add to the complexity. However, for the limited range investigated in this study, it is not expected that the difference is statistically meaningful. To obtain a more precise parameterization of the correlation, further variations in fan speed would be required. Following the linear regression approach, a correlation with a slope of 0.03 $W\,m^{-2}\,K^{-1}\,rpm^{-1}$ and an ordinate intercept of 30 $W\,m^{-2}\,K^{-1}$ was derived (Table 3). As expected, the dryer air temperature does not play a significant role in the mean heat transfer estimate, which strengthens the validity of the coefficient to emulate the physical drying behavior.

### 3.2 | Transfer of the Model to Another Pilot Plant Dryer

In the next step, the model was applied to a second pilot plant machine, which differs, among other factors, in section length, section volume, supply air volume flux, and circulating air volume flux. Figure 4 shows the thermocouple measurements and model results with mean heat-transfer coefficients to fit the drying time. Overall, the film temperature of the wet film measured by the thermocouple is slightly higher than in the model. A likely explanation is a slightly higher heat-transfer coefficient of the nozzles at the bottom of the web compared to the top of the web, as their distance is smaller and the impingement of the airflow is different. This would lead to a higher heat flux into the web from the bottom without increasing the mass-transfer coefficient at the top, which can slightly increase the film temperature. Another explanation would be measuring deviations of the thermocouple, for example, because it could be affected by the temperature of the dryer air, which is higher than the temperature of the wet film.

Increasing the ventilation power reduces the drying time, leading to an increase in the mean heat-transfer coefficient needed to fit the temperature curve in the model. When the dryer air temperature increases, the drying time is reduced without affecting the mean heat-transfer coefficient, which supports the fact that this empirical coefficient is not significantly affected by dryer temperature as its physical counterpart. Following the linear regression approach, a correlation between the mean convective heat-transfer coefficient and the ventilation power (in %) with a slope of 0.55 W $m^{-2}$ $K^{-1}$ % – pt.$^{-1}$ and an ordinate intercept of 17.2 W $m^{-2}$ $K^{-1}$ was derived from the six variations (Table 3).

These characterizations of the dryer can now be used to recalculate other dryer settings and to optimize for a certain product. In addition, multistage drying profiles in which the temperatures or the air flows of the dryer segments differ, as proposed in the literature to increase drying rate without compromising electrode quality [18], can also be implemented in the model by varying the dryer air temperature and fan speed or fan power in the segments accordingly.

Another strength of the model lies in its ability to calculate complete film temperature and film solvent content curves for any set of drying parameters. Its validity and versatility become apparent when applied to other experiments. In the supporting information (Chapter S4), the model is used to recalculate the drying profiles of experiments that involve the hybrid application of additional heating technologies from a previous study [23]. This provides detailed information about the drying process and the impact of additional heating, which would otherwise be difficult to obtain due to the complexity of the trials and the challenge of setting up sufficient measurements.

### 3.3 | Validation of the Drying Model

To further validate the dryer condition model, the measured exhaust dew point and the model exhaust dew point were compared. They show a linear correlation, which indicates that the dryer air condition model is depicting the main impacts properly (Figure 5A). However, especially at high drying rates, the model exhaust dew points are slightly higher than the measured dew points during the experiments. This may be due to the measurement setup. The dew point mirror has a response time of several

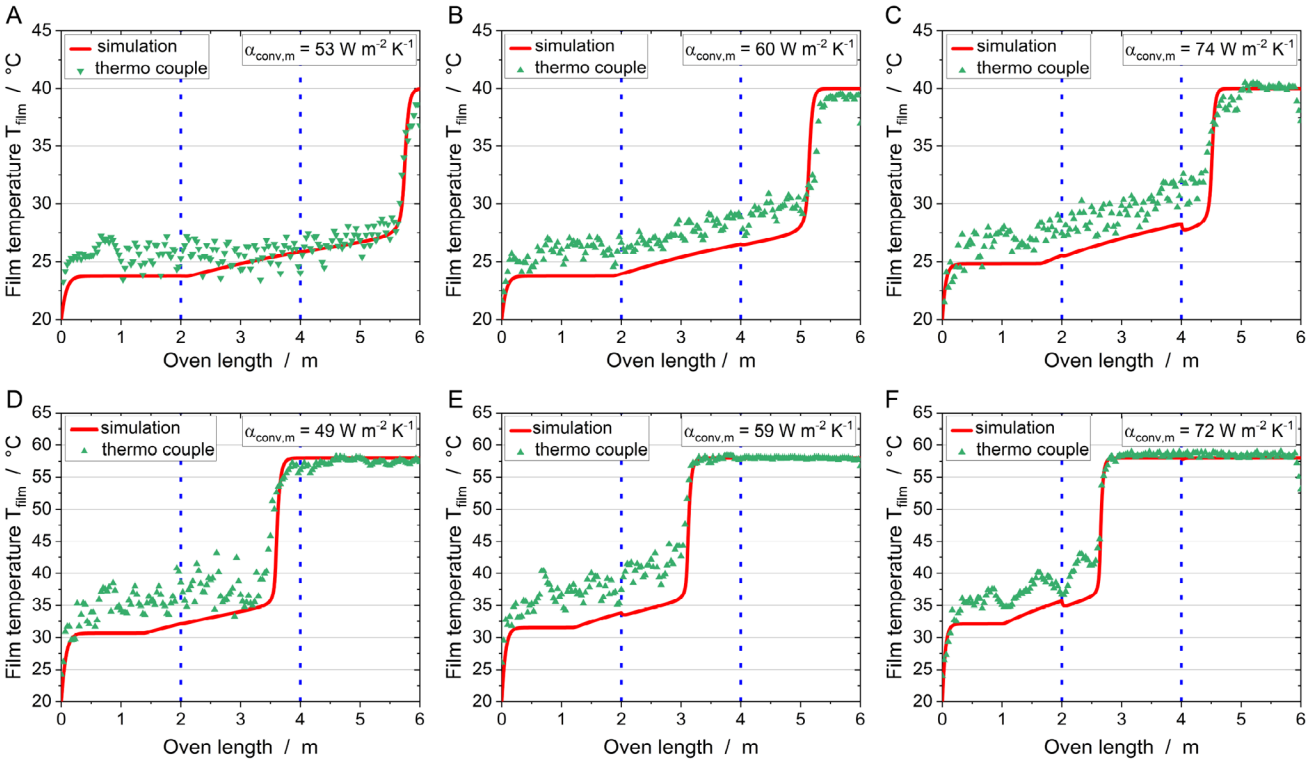


**FIGURE 4** | Film temperature for anode drying on the Kroenert machine measured with thermocouple and simulated with coupled drying model at iteratively selected $\alpha_{conv,m}$; variations of set points for $T_{dryer}$ and $P_{fan}$; (A–C) at 40°C and (D–F) 60°C; A, D at 60% and B, E at 80%, C, F at 100%, indications of segments (blue).

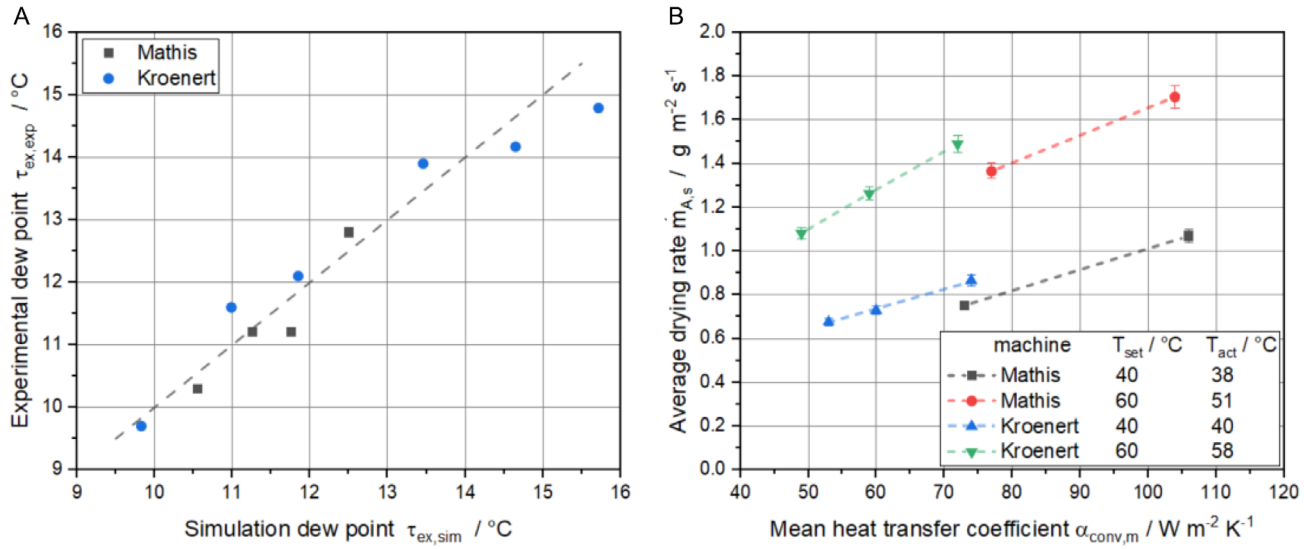


**FIGURE 5** | Validation of the model with experiment results: (A) exhaust dew point; (B) average drying rate versus mean heat-transfer coefficient. For the Mathis machine, the actual temperature deviated from the set temperature in case of the 60°C setting.

minutes, which is required for the mirror to reach the temperature needed to match the humidity of the measured air. The comparably short length of the applied coating per experiment of 10 m, equating to 5 min of coating time, may have been insufficient for an accurate measurement. Although the ambient dew point during the trials on the Kroenert machine was significantly lower than during the trials on the Mathis machine (Mathis 7.7 °C and Kroenert 3.2 °C), the amount of solvent in the exhaust air of the Kroenert machine is higher than in the exhaust air of the Mathis machine. This is due to differences in the rate of air exchange through air exhaust and fresh air supply.

In Figure 5B, the measured drying rate is plotted against the mean convective heat-transfer coefficient for each experiment. At a fixed dryer temperature, both machines exhibit essentially the same linear relationship, indicating that an increase in the heat-transfer coefficient produces a proportional increase in the drying rate. This trend follows directly from Lewis's analogy between heat- and mass-transfer coefficients (Equation (6)) together with the proportionality of the mass-transfer coefficient to the drying rate under the assumption of constant dryer air humidity (Equation (5)). The three main factors that influence the drying rate are the mean heat-transfer coefficient, $\alpha_{conv,m}$, the humidity of the dryer air, $Y_{s,dryer}$, and the actual dryer air temperature, $T_{act}$. At high drying rates, the humidity of the air increases significantly, especially in the case of the Kroenert machine. However, in the considered parameter range, no significant effect was observed. The actual dryer air temperatures in the Mathis dryer have been below the set temperature values, which notably leads to slightly lower drying rates compared to the Kroenert machine at similar settings for the mean heat-transfer coefficient. However, the impact is minor because the higher moisture content of the air in the Kroenert machine offsets the differences in dryer air temperature. The most important parameters for the compared experiments are given in Table 4. For further validation, the model was used to recreate the temperature curves for experiments on the same Mathis machine, performed in previous work, where the supply air dew point was significantly higher (up to 16 °C) [23]. The full production parameter set for these experiments can be found in Table S4. There was good agreement between the model and the experimental temperature data sets, highlighting that changes in the supply air moisture content affect the drying rate but do not affect the validity of the mean convective heat-transfer coefficient.

The good alignment of the simulation and experiment underlines the strength of the mean heat-transfer coefficients as a parameter to transfer the drying parameters from one machine to another. Furthermore, the results indicate that the model is capable of depicting the main impacts on the drying behavior of the anodes in different pilot plants and that the proposed model can be a valuable tool to transfer drying parameters between two different pilot plant dryers.

Similar drying kinetics are expected to deliver similar electrode quality. To verify this expectation for the anodes in this study, electrode quality measurements were carried out, revealing a similar correlation between the drying rate and the electrode quality for both pilot plants (Figure 6). The adhesion strength is an important intermediate quality parameter to ensure the processability of the electrodes in subsequent process steps. Therefore, it is common to evaluate the drying performance. The adhesion strength of the electrodes decreases as the mean drying rate increases. Low drying rates of 0.68 g m$^{-2}$ s$^{-1}$ lead to a high adhesion strength of 1.16 MPa. A high drying rate of 1.71 g m$^{-2}$ s$^{-1}$ led to a significantly lower adhesion strength of 0.7 MPa. This effect is well described in the literature and is related to evaporation-induced segregation of active and inactive components in the electrode, often referred to as "binder migration" [4, 20, 23]. When the adhesion strength of electrodes produced on the two machines is compared at the same average drying rate, the anodes from the Kroenert machine show slightly higher values. For example, at a drying rate of approximately 0.74 g m$^{-2}$ s$^{-1}$, the anodes of the Mathis machine exhibit an adhesion strength of 1.04 MPa, whereas the anodes of the Kroenert machine exhibit an adhesion strength of 1.12 MPa. At a drying rate of 1.07 g m$^{-2}$ s$^{-1}$, the anodes of the Mathis machine achieve an adhesion strength of 0.91 MPa, while the anodes of the Kroenert machine reach an adhesion strength of

**TABLE 4** | Model parametrization and validation; given are the used dryer model, the measured dryer air temperature, $T_{act}$, the fan speed or fan Power $n_{fan}/P_{fan}$, the mean convective heat-transfer coefficient, $\alpha_{conv,m}$, the dew points of the ambient/supply air, $\tau_{amb}$, the measured exhaust air, $\tau_{ex,exp}$, and the simulated exhaust air, $\tau_{ex,sim}$, and the average drying rates as measured, $\dot{m}_{A,s,exp}$, and simulated, $\dot{m}_{A,s,sim}$.

| dryer unit | $T_{act}$, °C | $n_{fan}/P_{fan}$, rpm/% | $\alpha_{conv,m}$, $Wm^{-2}K^{-1}$ | $\tau_{amb}$, °C | $\tau_{ex,exp}$, °C | $\tau_{ex,sim}$, °C | $\dot{m}_{A,s,exp}$, $gm^{-2}s^{-1}$ | $\dot{m}_{A,s,sim}$, $gm^{-2}s^{-1}$ |
|---|---|---|---|---|---|---|---|---|
| Mathis | 38 | 1500 | 73 | 7.7 | 10.3 | 10.56 | 0.752 | 0.8 |
| Mathis | 38 | 2500 | 106 | 7.7 | 11.2 | 11.26 | 1.069 | 1.054 |
| Mathis | 51 | 1500 | 77 | 7.7 | 11.2 | 11.76 | 1.365 | 1.268 |
| Mathis | 51 | 2500 | 104 | 7.7 | 12.8 | 12.51 | 1.705 | 1.683 |
| Kroenert | 40 | 60 | 53 | 3.2 | 9.7 | 9.83 | 0.675 | 0.670 |
| Kroenert | 40 | 80 | 60 | 3.2 | 11.6 | 10.99 | 0.729 | 0.727 |
| Kroenert | 40 | 100 | 74 | 3.2 | 12.1 | 11.85 | 0.866 | 0.854 |
| Kroenert | 58 | 60 | 49 | 3.2 | 13.9 | 13.46 | 1.083 | 1.062 |
| Kroenert | 58 | 80 | 59 | 3.2 | 14.2 | 14.65 | 1.264 | 1.241 |
| Kroenert | 58 | 100 | 72 | 3.2 | 14.8 | 15.72 | 1.490 | 1.450 |
| Mathis | 35 | 2500 | 105 | 14 | - | 16.75 | 0.813 | 0.781 |
| Mathis | 35 | 2000 | 90 | 14 | - | 16.53 | 0.739 | 0.691 |
| Mathis | 35 | 1500 | 75 | 14 | - | 16.28 | 0.626 | 0.596 |
| Mathis | 36 | 2500 | 105 | 16 | - | 17.16 | 0.879 | 0.942 |

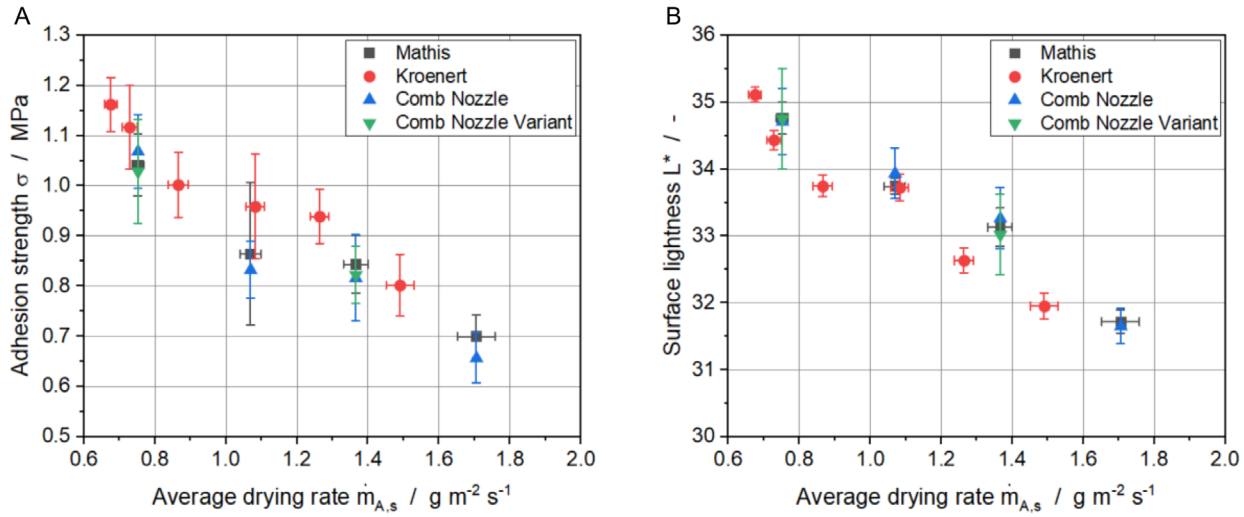


**FIGURE 6** | Comparison of the electrode quality in regard to the average drying rate from drying trials on the Mathis- and Kroenert-dryers; laboratory-scale results with the stationary dryer at constant (Comb Nozzle) and varying heat-transfer coefficients (same mean value, Comb Nozzle Variant) are also shown. (A) Adhesion strength and (B) surface lightness L*.

0.96 MPa. There are many possible reasons for the slight differences. Some reasons are not related to the machines themselves, such as deviations in the areal mass loading of the coatings [4, 31, 32] or small differences between the slurry batches used during the three coating trials. Variations in web tension or substrate handling between the machines could further influence adhesion strength [37]. Minor machine-specific effects may also contribute, such as differences in airflow uniformity or nozzle positioning, which can slightly change the drying profile even at the same nominal drying rate. Altvater et al. reported that differences in film temperature during the constant-rate period can affect electrode adhesion due to the temperature-dependent diffusion rate of the binder [13]. For the present study, this constant-rate film temperature is up to 5 °C higher for the Kroenert machine, providing a possible explanation for these slightly higher adhesion strengths. However, the standard deviations show a high degree of overlap, suggesting that these differences are not statistically meaningful.

The analysis of the color of the electrode powders, slurries, and coatings was proposed by Weber & Schoo et al. as an alternative quality parameter that can be obtained inline and nondestructively throughout the electrode production chain [32]. For coatings, they have shown that the carbon black content and the areal loading can be correlated with changes in surface lightness, L*. As shown in previous work, a reduction in surface lightness can also be detected for an increase in drying rate, attributed to the

increased concentration of dark carbon black particles close to the electrode surface due to the segregation effect described earlier [23]. This decrease in surface lightness as a consequence of an increase in the average drying rate also occurs in the anodes dried in this study, indicating carbon black concentration at the electrode surface. At low drying rates of about 0.68 g $m^{-2}$ $s^{-1}$, the surface lightness is high with a value of 35.1, whereas at high drying rates of 1.71 g $m^{-2}$ $s^{-1}$, it drops to 31.8. As for the adhesion strength, the surface lightness also reveals no significant difference between electrodes produced at similar drying rates in the two pilot plant machines, which underlines the principle transferability of the production between the pilot machines.

In addition to the pilot scale results, Figure 6 also presents the data obtained from the laboratory experiments. In the Comb Nozzle series, the heat-transfer coefficient was maintained at a constant value, whereas in the Comb Nozzle Variant series, it was periodically varied over the drying time to mimic the heat transfer profile characteristic of a roll-to-roll drying process. The temporal variation was derived from the nozzle spacing and web speeds corresponding to the operating points of the Mathis dryer. The time-averaged heat-transfer coefficient was identical to the constant value used in the comb nozzle experiments. As shown in Figure 6, the adhesion strength values obtained with the stationary laboratory dryer in both Comb Nozzle series closely follow the trend observed for electrodes produced on the two pilot-scale dryers. A very similar consistency is observed for the corresponding surface lightness. Accordingly, at identical film temperatures and average heat-transfer coefficients, as determined by the drying model for the Mathis machine, electrodes of comparable quality in terms of adhesion strength and surface lightness are achieved. Except for the low drying rate of 0.74 g $m^{-2}$ $s^{-1}$ in the Comb Nozzle test series, the adhesion strength values measured in the laboratory experiments are slightly lower than those of the Mathis dryer in both the Comb Nozzle and Variant series. Because these very small differences fall within the experimental standard deviation and are not accompanied by differences in surface lightness, they are most likely attributed to measurement uncertainties and are not discussed further. Consequently, the comparable electrode quality at identical average drying rates can be attributed to the fact that, despite the different scales (pilot versus laboratory), similar drying kinetics are present. Therefore, this finding indicates, firstly, that the average heat-transfer coefficients derived from the drying model are valid, and secondly, that scaling up from laboratory to pilot-line is feasible. However, such a scale-up requires complete characterization of the dryer, as performed in this study.

The comparison of the two Comb Nozzle experimental series further confirms that a time-dependent heat- and mass-transfer profile has no significant effect on the electrode properties. It is possible that the limited variance of heat (and mass) transfer coefficients in the laboratory dryer contributed to this observation. In the experiments, the difference between the maximum and minimum heat-transfer coefficients was approximately 50 W $m^2$ $K^{-1}$, while in pilot-scale dryers this difference can reach several hundred W $m^2$ $K^{-1}$ [26]. However, taken together, the results suggest that temporal variations in the heat- and mass-transfer coefficients play a rather negligible role in determining the electrode properties under the investigated conditions. This conclusion is further supported by the results derived from the two pilot-scale dryers, in which variations in nozzle spacing generate heat- and mass-transfer profiles that vary both spatially and temporally. Despite these differences, comparable electrode properties were obtained at identical average drying rates. The absence of a heat- and mass-transfer profile effect in the pilot dryers may be related to the staggered arrangement of nozzles on the top and bottom surfaces. Consequently, energy input from a bottom-side nozzle occurs precisely between two top-side nozzles, which could influence the results. Accordingly, the approximation of the drying process using average heat- and mass-transfer coefficients appears to be a suitable approach. The validation across a laboratory dryer and two different pilot-scale dryers, including trials using additional heating technologies (chapter S4), implies that a transfer to different dryer designs or drying scenarios is generally possible. The dryer condition model may require modification to accurately reflect the specific airflow configuration of the dryer. This may include, among other factors, accounting for missing air-recirculation paths or integrating additional dehumidification units. Furthermore, the model is applicable to other solvents, such as N-2-methylpyrrolidone (NMP), which is commonly used for cathode coatings. For such applications, the electrode-drying model must be parameterized to account for the different material and solvent properties. This includes, but is not limited to, heat capacity, thermal conductivity, diffusion coefficients, heat of vaporization, vapor pressure, and the sorption behavior of the solvent.

## 4 | Conclusion

Ramping up the production of batteries is costly and time-consuming due to the challenges involved in transferring results from the laboratory to pilot lines and into industrial production. In particular, achieving the desired throughput and necessary quality in electrode production may require several test runs, resulting in scrap and associated costs. In order to successfully transfer the electrode drying parameter set from the laboratory to the pilot scale and between different roll-to-roll coating lines, it is necessary to match the fundamental driving forces that control film temperature and drying rate. The film temperature regulates surface vapor pressure and diffusion kinetics, while the drying rate balances solvent evaporation and internal diffusion to prevent concentration gradients of components in the electrode. These two metrics are both governed by four interdependent physical levers: the heat- and mass-transfer coefficients arising from airflow distribution; the drying air temperature, which may vary, especially at the end of the dryers where cold air is sucked in; and the dryer air humidity, which is determined by the fresh air fraction, recirculation, and ongoing solvent evaporation. The limited direct control of local transfer coefficients, combined with operational fluctuations in moisture content of the air, means that simply duplicating the parameter set is insufficient for reliable scale-up. This is especially the case when transferring between machines from different suppliers, where identical setpoints may not exist due to differences in control functions. To address these challenges, a physics-based drying model, which was originally developed for laboratory-scale anode coatings, was adapted to two convective pilot-plant dryers. A coupled dryer-air conditioning sub-model was used to capture solvent enrichment in the circulating air and its effect on the drying rate. Applying a single mean heat-transfer coefficient to each

experimental run allowed the wet-film temperature profile to be reproduced and the exhaust-air dew points to be accurately predicted. The strong correlations among the fitted coefficients, dryer air temperature, humidity, and measured drying rates confirmed that these unified parameters capture the dominant drying kinetics. A quantitative relationship between fan speed and fan power, respectively, and the mean heat-transfer coefficient of each dryer was approximated by linear regression of a limited number of parametrization trials. These relationships enable a direct transfer of operating settings between both pilot platforms, and comparable drying rates and electrode quality were achieved. Furthermore, applying the same derived parameters to a discontinuous laboratory-scale dryer produced equivalent electrode quality, demonstrating the ability to describe the complex dryer sufficiently well using this unified mean heat-transfer coefficient. To parameterize the drying model of each dryer, several drying experiments at varying parameter sets and measurements of all relevant air flux are needed. However, this approach does not require detailed knowledge about all internal geometries of the drying chamber or complex CFD simulations. This reduction in complexity may be a time-saving approach for the scale-up of battery electrode drying. For practical deployment in an industrial context, the approach can be implemented in two steps. First, the pilot dryer and the target industrial dryer are characterized through a limited set of drying experiments at homogeneous parameter settings to parameterize the model and identify the relationship between the air-flow control settings and the resulting mean convective heat-transfer coefficient. Second, drying profiles validated on the pilot line can be transferred directly to the industrial dryer, with only minor adjustments expected, which reduces iterative trial-and-error during process setup. In addition, the calibrated model can serve as a rudimentary digital twin of the dryer, enabling rapid adaptation of drying profiles to changes in coating formulations, solids content, solvents, or areal mass loadings. These findings establish a robust quantitative framework for translating drying parameter sets across scales. Focusing on the underlying thermodynamic drivers rather than machine-specific setpoints promises to accelerate scale-up and reduce the scrap and the overall cost during the process.

## Author Contributions

**Max-Wolfram von Horstig**: data curation (lead), investigation (lead), methodology (lead), validation (lead), visualization (lead), writing – original draft (lead). **Julian Borho**: investigation (supporting), writing – original draft (supporting). **Jonas Mohacsi**: writing – original draft (supporting), writing – review & editing (supporting). **Philip Scharfer**: writing – review & editing (lead). **Peter Michalowski**: funding acquisition (supporting), writing – review & editing (supporting). **Wilhelm Schabel**: supervision (lead), writing – review & editing (supporting). **Arno Kwade**: funding acquisition (lead), supervision (lead), writing – review & editing (lead).


## Acknowledgements

Open Access funding enabled and organized by Projekt DEAL.

## Funding

This publication was supported by two projects funded by the German federal government: the "Next-Generation of Power Batteries" (NEWBIE) project, financed by the Federal Ministry for Economic Affairs and Energy under grant number 01MV21013A, and the "Modernization of BLB Electrode Production" (ModElPro) project, funded by the Federal Ministry of Education and Research under grant number 03XP0424. The authors are responsible for the content of this publication.


## Conflicts of Interest

The authors declare no conflicts of interest.

## Data Availability Statement

The data that support the findings of this study are available from the corresponding author upon reasonable request.

## References


1. M. Schütte, F. Degen, and H. Walter, "Reducing Energy Consumption and Greenhouse Gas Emissions of Industrial Drying Processes in Lithium-Ion Battery Cell Production: A Qualitative Technology Benchmark," *Batteries* 10 (2024): 64.

2. N. von Drachenfels, J. Husmann, U. Khalid, F. Cerdas, and C. Herrmann, "Life Cycle Assessment of the Battery Cell Production: Using a Modular Material and Energy Flow Model to Assess Product and Process Innovations," *Energy Technology* 11, no. 5 (2023): 2200673.

3. B. G. Westphal and A. Kwade, "Critical Electrode Properties and Drying Conditions Causing Component Segregation in Graphitic Anodes for Lithium-Ion Batteries," *Journal of Energy Storage* 18 (2018): 509–517.

4. S. Jaiser, N. Salach, M. Baunach, P. Scharfer, and W. Schabel, "The Impact of Drying Conditions and Wet Film Properties on Adhesion and Film Solidification of Lithium Ion Battery Anodes," *Drying Technology* 35 (2017): 1807–1817.

5. J. Kumberg, W. Bauer, J. Schmatz, et al., "Reduced Drying Time of Anodes for Lithium-Ion Batteries through Simultaneous Multilayer Coating," *Energy Technology* 9, no. 10 (2021): 2100367.

6. L. Gottschalk, C. Oertel, N. Strzelczyk, et al., "Improving the Performance of Lithium-Ion Batteries Using a Two-Layer, Hard Carbon-Containing Silicon Anode for use in High-Energy Electrodes," *Energy Technology* 11, no. 5 (2023): 2200858.

7. S. B. Seo, Y. Song, Y. R. Choi, et al., "Double-Walled Carbon Nanotubes as Effective Conducting Agents for Lithium Iron Phosphate Cathodes," *Carbon* 218 (2024): 118731.

8. J.-M. Kim, S.-H. Kim, N. Y. Kim, et al., "Nanofibrous Conductive Binders Based on Dna-Wrapped Carbon Nanotubes for Lithium Battery Electrodes," *iScience*, 23 (2020): 101739.

9. S. Ritu, D. L. Woof III, K. Alexander, M. G. Kelsey, L. Jianlin, and I. Belharouak, "Towards Understanding of Cracking during Drying of Thick Aqueous-Processed Lini0.8mn0.1co0.1o2 Cathodes," *ACS Sustainable Chemistry & Engineering* 8, no. 8 (2020): 3162–3169.

10. E. Wiegmann, A. Kwade, and W. Haselrieder, "Solvent Reduced Extrusion-Based Anode Production Process Integrating Granulate Coating, Drying, and Calendering," *Energy Technology* 10, no. 6 (2022): 2200020.

11. J. Offermann, E. Gayretli, C. Schmidt, et al., "Enabling High-Performance Battery Electrodes by Surface-Structuring of Current Collectors and Crack Formation in Electrodes: A Proof-of-Concept," *Journal of Colloid and Interface Science* 664 (2024): 444–453.

12. H. Jeong, J. Jang, and C. Jo, "A Review on Current Collector Coating Methods for Next-Generation Batteries," *Chemical Engineering Journal* 446 (2022): 136860.

13. A. Altvater, T. Heckmann, J. C. Eser, S. Soiegel, P. Scharfer, and W. Schabel, "(Near-) Infrared Drying of Lithium-Ion Battery Electrodes: Influence of Energy Input on Process Speed and Electrode Adhesion," *Energy Technology* 11, 2022.

14. S. Fink, D. Demir, M. Börner, V. Göken, and C. Vedder, "High-Speed Laser Drying of Lithium-Ion Battery Anodes: Challenges and Opportunities," *World Electric Vehicle Journal* 14, no. 9 (2023): 255.

15. D. Neb, S. Kim, H. Clever, B. Dorn, and A. Kampker, "Current Advances on Laser Drying of Electrodes for Lithium-Ion Battery Cells," *Procedia CIRP* 107 (2022): 1577–1587.

16. H. Wang, Y. Chen, Y. Song, and D. Xiong, "Rapid Electrode Drying for High-Quality Lithium-Ion Batteries: A Three-Stage Laser Irradiation Method," *Journal of Energy Storage* 118 (2025): 116288.

17. M.-W. von Horstig, A. Schoo, T. Loellhoeffel, J. K. Mayer, and A. Kwade, "A Perspective on Innovative Drying Methods for Energy-Efficient Solvent-Based Production of Lithium-Ion Battery Electrodes," *Energy Technology* 10 (2022): 2200689.

18. S. Jaiser, A. Friske, M. Baunach, P. Scharfer, and W. Schabel, "Development of a Three-Stage Drying Profile Based on Characteristic Drying Stages for Lithium-Ion Battery Anodes," *Drying Technology* 35, no. 10 (2017): 1266–1275.

19. M. Keppeler, H.-Y. Tran, and W. Braunwarth, "The Role of Pilot Lines in Bridging the Gap between Fundamental Research and Industrial Production for Lithium-Ion Battery Cells Relevant to Sustainable Electromobility: A Review," *Energy Technology* 9, no. 8 (2021): 2100132.

20. S. Jaiser, M. Müller, M. Baunach, W. Bauer, P. Scharfer, and W. Schabel, "Investigation of Film Solidification and Binder Migration during Drying of Li-Ion Battery Anodes," *Journal of Power Sources* 318 (2016): 210–219.

21. J. Kumberg, M. Baunach, J. Eser, A. Altvater, P. Scharfer, and W. Schabel, "Investigation of Drying Curves of Lithium-Ion Battery Electrodes with a New Gravimetrical Double-Side Batch Dryer Concept including Setup Characterization and Model Simulations," *Energy Technology* 9 (2021): 2000889.

22. J. Kumberg, M. Baunach, J. Eser, A. Altvater, P. Scharfer, and W. Schabel, "Influence of Layer Thickness on the Drying of Lithium-Ion Battery Electrodes—simulation and Experimental Validation," *Energy Technology* 9 (2021): 202100013.

23. M.-W. von Horstig, C. Zhang, G. V. Silva, P. Michalowski, C. Herrmann, and A. Kwade, "Induction vs. Laser Heating: A Comparative Study on Innovative Electrode Drying Technologies on Pilot-Scale," *Journal of Power Sources* 654 (2025): 237780.

24. C. Zirhul, M. Lippke, and A. Kwade, "Binder Migration during Drying of Lithium-Ion Battery Electrodes: Modelling and Comparison to Experiment," *Batteries* 9, no. 9 (2023): 177–185.

25. F. Font, B. Protas, G. Richardson, and J. M. Foster, "Binder Migration during Drying of Lithium-Ion Battery Electrodes: Modelling and Comparison to Experiment," *Journal of Power Sources* 393 (2018): 177–185.

26. T. Nienke, H. Embrechts, A. Kwade, and D. Eggerath, "Experimental and Numerical Investigation of the Influence of Nozzle Design on the Industrial Convection Drying of Thin Films," *Drying Technology* 40, no. 13 (2022): 2685–2695.

27. C. Zhao, Y. Zhang, X. Du, J. Zhao, and Y. Hu, "Modeling and Analysis of the Drying Process of Lithium-Ion Battery Electrodes Based on Non-Steady-State Drying Kinetics," *Processes* 11, no. 11 (2023): 3236.

28. Y. Guo, J. Tan, M. Zhang, et al., "A Review of Heat and Mass Transfer during Drying of Lithium-Ion Battery Electrodes," *Science China Technological Sciences* 68, no. 10 (2025): 2010101.

29. T. Nienke, J. S. Gomez Bonilla, A. Kwade, and D. Eggerath, "Combination of Different Nozzle Concepts for Simultaneous Optimization of Heat Transfer and Its Uniform Distribution in Convection Drying Applications," *Drying Technology* 42, no. 1 (2024): 48–60.

30. M.-W. von Horstig, R. Moschner, O. Landrath, P. Michalowski, and A. Kwade, "Development of an Induction Supported Roll to Roll Process for the Accelerated Drying of Water-Based Anodes and n-Methyl-2-Pyrrolidone-Based Cathodes for Lithium-Ion Batteries," *Energy Technology* 13 (2025): 2402182.

31. W. Haselrieder, B. Westphal, H. Bockholt, A. Diener, S. Höft, and A. Kwade, "Measuring the Coating Adhesion Strength of Electrodes for Lithium-Ion Batteries," *International Journal of Adhesion and Adhesives* 60 (2015): 1-8.

32. M. Weber, A. Schoo, M. Sander, J. Burmeister, and A. Kwade, "Introducing Spectrophotometry for Quality Control in Lithium-Ion-Battery Electrode Manufacturing," *Energy Technology* 11 (2023): 2201083.

33. A. Kwade, W. Haselrieder, R. Leithoff, A. Modlinger, F. Dietrich, and K. Droeder, "Current Status and Challenges for Automotive Battery Production Technologies," *Nature Energy* 3 (2018): 290–300.

34. X. Ye, Z. Yang, X. Liu, Q. Lu, S. Yuan, and F. Jiang, "Optimizing Porous Medium Electrode Suspension Drying: A Numerical Simulation," *Physics of Fluids* 36, no. 7 (2024): 07.

35. M. Stein IV, A. Mistry, and P. P. Mukherjee, "Mechanistic Understanding of the Role of Evaporation in Electrode Processing," *Journal of the Electrochemical Society* 164 (2017): A1616–A1627.

36. P. Stephan, S. Kabelac, M. Kind, D. Mewes, K. Schaber, and T. Wetzel, eds. *ISBN. 978-3-662-52988-1. 1.-6. Aufl. VDI-Verlag GmbH, Düsseldorf; 7.-11. Aufl*, 12th ed. (Springer Reference Technik, Springer Vieweg, 2019).

37. M. Kim, J. Noh, S. Lee, J. Yun, and C. Lee, "Mitigating Strain Deviation by Investigating Tension Transfer Mechanisms Dependent on Anode Shape in Roll-to-Roll Electrode Fabrication," *Structural and Multidisciplinary Optimization* 68, no. 9 (2025): 184.

## Supporting Information

Additional supporting information can be found online in the Supporting Information section.